

This is the accepted manuscript made available via CHORUS. The article has been published as:

# Scalewise invariant analysis of the anisotropic Reynolds stress tensor for atmospheric surface layer and canopy sublayer turbulent flows

Peter Brugger, Gabriel G. Katul, Frederik De Roo, Konstantin Kröniger, Eyal Rotenberg, Shani Rohatyn, and Matthias Mauder

Phys. Rev. Fluids **3**, 054608 — Published 24 May 2018

DOI: [10.1103/PhysRevFluids.3.054608](https://doi.org/10.1103/PhysRevFluids.3.054608)

# Scalewise invariant analysis of the anisotropic Reynolds stress tensor for atmospheric surface layer and canopy sublayer turbulent flows

Peter Brugger,<sup>1,\*</sup> Gabriel G. Katul,<sup>2,3,4</sup> Frederik De Roo,<sup>1</sup> Konstantin Kröniger,<sup>1</sup> Eyal Rotenberg,<sup>5</sup> Shani Rohatyn,<sup>5</sup> and Matthias Mauder<sup>1</sup>

<sup>1</sup>Karlsruhe Institute of Technology (KIT), Institute of Meteorology and Climate Research - Atmospheric Environmental Research (IMK-IFU), Kreuzeckbahnstrae 19, 82467 Garmisch-Partenkirchen, Germany

<sup>2</sup>Nicholas School of the Environment, Box 80328, Duke University, Durham, NC 27708, USA

<sup>3</sup>Department of Civil and Environmental Engineering, Duke University, Durham, NC 27708, USA

<sup>4</sup>Karlsruhe Institute of Technology (KIT), Institute of Meteorology and Climate Research - Atmospheric Environmental Research (IMK-IFU), Kreuzeckbahnstraße 19, 82467 Garmisch-Partenkirchen, Germany

<sup>5</sup>Weizmann Institute of Science (WIS), Faculty of Chemistry, Department of Earth and Planetary Sciences, 234 Herzl Street, Rehovot 7610001, Israel  
(Dated: April 27, 2018)

Anisotropy in the turbulent stress tensor, which forms the basis of invariant analysis, is conducted using velocity time series measurements collected in the canopy sublayer (CSL) and the atmospheric surface layer (ASL). The goal is to assess how thermal stratification and surface roughness conditions simultaneously distort the scale-wise relaxation towards isotropic state from large to small scales when referenced to homogeneous turbulence. To achieve this goal, conventional invariant analysis is extended to allow scale-wise information about relaxation to isotropy in physical (instead of Fourier) space to be incorporated. The proposed analysis show that the CSL is more isotropic than its ASL counter part at large, intermediate, and small (or inertial) scales irrespective of the thermal stratification. Moreover, the small (or inertial) scale anisotropy is more prevalent in the ASL when compared to the CSL, a finding that cannot be fully explained by the intensity of the mean velocity gradient acting on all scales. Implications to the validity of scale-wise Rotta and Lumley models for return-to-isotropy as well as advantages to using barycentric instead of anisotropy invariant maps for such scale-wise analysis are discussed.

## I. INTRODUCTION

The classical treatment of turbulence in the atmospheric surface layer (ASL) and the roughness sublayer (CSL) above canopies has primarily focused on distortions to the mean velocity profile caused by the presence of roughness elements and thermal stratification [1–9]. Surface roughness effects and thermal stratification modify the components of the Reynolds stress tensor as evidenced by a large number of experiments and simulations [5, 10–19]. These modifications are expected to lead to differences in kinetic energy distribution among velocity components comprising the stress tensor. Such differences in energy anisotropy has been previously used to explore the sensitivity of turbulent structures to surface boundary conditions such as roughness changes [20–25] or thermal stratification [26]. However, the route of how the anisotropy at large scales relaxes to quasi-isotropic state at small scales remains a subject of research [27–31]. The juxtaposition of these questions and studies to ASL and CSL turbulence using field measurements is the main motivation for the work here.

Exchanges of turbulent kinetic energy among the three spatial components occur through interactions between fluctuating velocities and pressure. Starting from an

anisotropic stress tensor  $\overline{u_i u_j}$ , these exchanges have been labeled as return-to-isotropy; when mean flow gradients are removed or suppressed, they describe the expected state that turbulence relaxes to. Here,  $u_i$  are the turbulent or fluctuating velocity components along  $x_i$ , where  $x_1$  (or  $x$ ),  $x_2$  (or  $y$ ), and  $x_3$  (or  $z$ ) represent the longitudinal, lateral, and vertical directions, respectively, overbar is time averaging and  $\overline{u_i} = 0$ . Much progress has been made by exploring connections between  $\overline{u_i u_j}$  and the so-called invariant analysis [22, 30, 32–36]. Such connections resulted in nonlinear models for the slow part of the pressure-strain correlation and highlighted distinct routes along which turbulence relaxes to isotropic conditions [27, 33, 34]. These routes have been succinctly summarized in what is labeled as anisotropy invariant maps (AIM) proposed by Lumley [33, 34]. Invariant analysis is based on the anisotropic second-order normalized stress tensor related to  $\overline{u_i u_j}$  by

$$a_{ij} = \frac{\overline{u_i u_j}}{2k} - \frac{1}{3}\delta_{ij}; k = \frac{\overline{u_m u_m}}{2}, \quad (1)$$

where  $k$  is the mean turbulent kinetic energy and  $\delta_{ij}$  is the Kronecker delta. This tensor has three invariants  $I_1 = a_{ii} = 0$  here,  $I_2 = a_{ij}a_{ji}$ , and  $I_3 = a_{ij}a_{jn}a_{ni}$ , where  $I_2$  and  $I_3$  can be linked to the three eigenvalues of  $a_{ij}$  (summarized later) and are independent of the reference system. Invariant maps feature  $I_3$  (abscissa) versus  $-I_2$  (ordinate) along with bounds imposed by realizability constraints on  $\overline{u_i u_j}$  (e.g.  $\det[a_{ij}] \geq 0$ , where

\* peter.bugger@kit.edu

det[.] is the determinant). The  $I_2$  represents the degree of anisotropy whereas  $I_3$  represents the nature (or topology) of the anisotropy. The AIM approach suggests that anisotropy in  $\overline{u_i u_j}$  may be 1-component (prolate energy distribution), 2-component (oblate energy distribution), or in all 3-components of which the isotropic state (spherical energy distribution) is a limiting case. Depending on the sign of  $I_3$ , progression from 1-component or 2-component to 3-component follows an axisymmetric expansion or contraction on the AIM when the source of inhomogeneity (e.g. mean flow gradients) is removed until isotropy is achieved [34]. As earlier noted, the AIM domain bounds all realizable Reynolds stress invariants [22, 34, 37, 38] thereby making AIM an effective visual tool to track anisotropy at different heights in boundary layer turbulence. In fact, the AIM proved to be effective at demonstrating that rough-wall turbulence appears more isotropic than its smooth-wall counterpart for the same Reynolds numbers [21]. Experiments and simulations [25] also reported that the AIM signature for smooth wall turbulence appears well defined and robust to variations in Reynolds number. The same experiments further showed that turbulent flows over 3-D  $k$ -type roughness appear more isotropic than flows over their 2-D  $k$ -type roughness counterpart throughout the boundary layer [25].

An alternative to the AIM representation is the barycentric map (BAM), which offers a number of advantages over AIM like non-distorted visualization of anisotropy and weighting of the limiting states as discussed elsewhere [32]. However, AIM and BAM representations are connected by transformations derived from the three eigenvalues of  $a_{ij}$ . Invariant analysis in  $a_{ij}$  assumes that anisotropy is inherently a large-scale feature and finer scales become isotropic and decoupled from their anisotropic large scales counterpart. How anisotropy in  $a_{ij}$  is destroyed as eddy sizes or scales become smaller remains a subject of inquiry, especially in vertically inhomogeneous flows characterizing the ASL and CSL of the atmosphere. The ASL and CSL experience mechanical production of  $k$  through interactions between the turbulent shear stress and the mean velocity profile. However, additional sources (or sinks) of  $k$  occur through surface heating (or cooling) and their associated thermal stratification. Above and beyond these two processes, canopy roughness effects introduce additional length scales (e.g. adjustment length and shear length scales) when describing flow statistics in the CSL [5, 39].

Two early pioneering attempts to extend invariant analysis across scales have been conducted in Fourier domain. One utilized numerical simulations of isotropic turbulence [28]. The other considered 3-component velocity time series collected in a pipe at multiple distances from the pipe-wall and at two bulk Reynolds numbers [23]. The simulation study showed that small-scale anisotropy in Reynolds stresses persisted and was traced back to non-local triad interactions that appear not efficient at

destroying an initial span-wise energy injection. The pipe flow experiments showed that at large scales, near-wall structures exhibit 'rod-like' (or prolate) energy distribution where as 'disk-like' (or oblate) energy distribution characteristics were reported as the buffer region is approached. Approximate isotropic states were reported as the pipe center is approached, where the mean velocity gradients approach zero (by virtue of symmetry). Another recent study [26] also extended aspects of invariant analysis across scales in the Fourier domain to explore how thermal stratification modifies isotropic and anisotropic states above an urban canopy. This work showed that the relaxation rate towards local isotropy varies with thermal stratification. Specifically, unstable atmospheric stability appears to be closer to isotropic state than its near-neutral or stable counterpart at a given scale or wavenumber. A relation was suggested between the scale over which maximum isotropy is attained and an outer length scale derived from temperature statistics [26].

The work here uses invariant analysis across scales in the ASL and CSL to explore the simultaneous role of roughness contrast and thermal stratification on anisotropy relaxation towards quasi-isotropic conditions. How anisotropy in  $a_{ij}$  produced at large scales varies with thermal stratification in the ASL and CSL, and how such large-scale anisotropic state relaxes to quasi-isotropic conditions at progressively smaller scales frame the scope of the work. The novelties of the analysis proposed here over prior work [23, 26] are that: 1) velocity differences in physical space are used instead of spectral and co-spectral analysis, and 2) both AIM and BAM measures of anisotropy are employed and their outcome compared to conventional local isotropy analysis. Advantages to conducting the analysis in physical space instead of spectral space are discussed.

With regards to the experimental design, the 3-component velocity time series have been simultaneously collected in the CSL above a tall forest and in the ASL above an adjacent desert-like shrubland. The runs span a wide range of atmospheric stability conditions as characterized by the atmospheric stability parameter. Distances to the surface or zero-plane displacement (in the case of the forest) are similar for both setups and are chosen to be commensurate with the aforementioned experiment on the urban surface layer [26]. It is envisaged that the analysis reported here offers a new perspective on the relative sensitivity of turbulent structures to roughness modifications and thermal stratification, especially at the cross-over from large (or integral) scales to inertial scales.

## II. METHOD OF ANALYSIS

### A. Definitions and Nomenclature

Any three dimensional second rank tensor  $\sigma_{ij}$  has three independent invariant quantities associated with it, which can be determined from the eigenvalues of  $\sigma_{ij}$ . The eigenvalues ( $\lambda$ ) are computed from the determinant  $\det[\sigma_{ij} - \lambda\delta_{ij}] = 0$ . Expanding the determinant of the matrix

$$\begin{bmatrix} \sigma_{11} - \lambda & \sigma_{12} & \sigma_{13} \\ \sigma_{21} & \sigma_{22} - \lambda & \sigma_{23} \\ \sigma_{31} & \sigma_{32} & \sigma_{33} - \lambda \end{bmatrix}$$

and setting it to zero yields the characteristic equation that defines the invariants and is given by [40]

$$\det[\sigma_{ij} - \lambda\delta_{ij}] = -\lambda^3 + I_1\lambda^2 - I_2\lambda + I_3 = 0, \quad (2)$$

where

$$I_1 = \sigma_{kk} = \text{tr}[\sigma] \quad (3)$$

$$I_2 = \frac{1}{2}(\sigma_{ii}\sigma_{jj} - \sigma_{ij}\sigma_{ji}) \quad (4)$$

$$I_3 = \det[\sigma_{ij}], \quad (5)$$

with  $\text{tr}[\cdot]$  being the trace of  $\sigma_{ij}$ . When  $\sigma_{ij} = a_{ij}$ , symmetry insures that equation 2 has three real roots (the eigenvalues) labeled as  $\lambda_1$ ,  $\lambda_2$ , and  $\lambda_3$ . The principal stresses are defined as components of  $\sigma_{ij}$  when the basis is changed so that the shear stress components become zero and  $\sigma_{ij}$  becomes a  $3 \times 3$  diagonal matrix whose elements are  $\sigma_1$ ,  $\sigma_2$ , and  $\sigma_3$ . These principal stresses are the three eigenvalues ordered by magnitude using  $\sigma_1 = \max(\lambda_1, \lambda_2, \lambda_3)$ ,  $\sigma_3 = \min(\lambda_1, \lambda_2, \lambda_3)$ , and  $\sigma_2 = I_1 - \sigma_1 - \sigma_3$ . The  $\sigma_1$ ,  $\sigma_2$ , and  $\sigma_3$  are independent of the coordinate basis in which the components of  $\sigma_{ij}$  are originally derived, which is advantageous in ASL and CSL field studies where large variations in wind directions are unavoidable. Applying the diagonal form of  $\sigma_{ij}$  to the definitions of the three invariants given by equation 2 yields the following simplified expressions

$$I_1 = \sigma_1 + \sigma_2 + \sigma_3 \quad (6)$$

$$I_2 = \sigma_1\sigma_2 + \sigma_2\sigma_3 + \sigma_3\sigma_1 \quad (7)$$

$$I_3 = \sigma_1\sigma_2\sigma_3. \quad (8)$$

These definitions directly apply to  $a_{ij}$  or any other second-rank tensor such as the strain rate [40, 41] and others relevant to vorticity and dissipation [20]. One advantage to using  $a_{ij}$  here instead of  $\overline{u_i u_j}$  for invariant analysis is that  $I_1 = \text{tr}[a_{ij}] = a_{11} + a_{22} + a_{33} = 0$  and only the second and third invariants are required.

The BAM framework makes use of the fact that  $a_{ij}$  can be expressed as a linear combination of three limiting states (1-component, 2-component, or 3-component). That is,  $a_{ij}$  can be decomposed into  $C_{1c}a_{1c} + C_{2c}a_{2c} +$

$C_{3c}a_{3c}$ , where  $C_{1c}$ ,  $C_{2c}$ , and  $C_{3c}$  are determined from the eigenvalues using [32]

$$C_{1c} = \lambda_1 - \lambda_2 \quad (9)$$

$$C_{2c} = 2(\lambda_2 - \lambda_3) \quad (10)$$

$$C_{3c} = 3\lambda_3 + 1, \quad (11)$$

and  $a_{1c}$ ,  $a_{2c}$ , and  $a_{3c}$  are  $3 \times 3$  diagonal matrices with diagonal elements  $[2/3, -1/3, -1/3]$  (1-component limiting state),  $[1/6, 1/6, -1/3]$  (2-component limiting state), and  $[0, 0, 0]$  (3-component limiting state). In the BAM representation,  $C_{1c}$ ,  $C_{2c}$ , and  $C_{3c}$  determined from  $\lambda_1$ ,  $\lambda_2$ , and  $\lambda_3$  indicate how much each turbulent state is contributing to a point situated in the map. The map itself can be constructed within an equilateral triangle with vertices being the three limiting states defined by coordinates  $(x_{1c}, y_{1c}) = (1, 0)$ ,  $(x_{2c}, y_{2c}) = (-1, 0)$ , and  $(x_{3c}, y_{3c}) = (0, 1)$ . Once these limiting states are set, a normalization is applied so that  $C_{1c} + C_{2c} + C_{3c} = 1$  and the coordinates of any point on the map  $(x_{BAM}, y_{BAM})$  can be determined from

$$x_{BAM} = C_{1c}x_{1c} + C_{2c}x_{2c} + C_{3c}x_{3c} \quad (12)$$

$$y_{BAM} = C_{1c}y_{1c} + C_{2c}y_{2c} + C_{3c}y_{3c}. \quad (13)$$

As discussed elsewhere [32], an equilateral triangle shaped BAM does not introduce any visual bias of the limiting states as is the case for the AIM. Randomly distributed points within BAM, when converted to AIM, result in visual clustering near the isotropic or 3-component state primarily because of the nonlinearity in the transformation from BAM to AIM.

### B. Measures of Anisotropy

A scalar measure of anisotropy in the AIM is the shortest or linear distance to the isotropic state. This distance was determined from  $I_2$  and  $I_3$  via [22, 33]

$$F = 1 + 27I_3 + 9I_2. \quad (14)$$

Isotropic turbulence is strictly attained when both  $I_2 = I_3 = 0$  and  $F = 1$ , whereas  $F = 0$  occurs along the linear boundary describing the 2-component state. The distance  $F$  was reported to be a function of distance from a solid boundary for various turbulent boundary layer flows [22–25]. At all distances from the boundary,  $F$  was smaller for turbulent flows over smooth wall when compared to all types of rough-wall cases [24, 25].

In the BAM, the distance to the isotropic state is [32]

$$C_{ani} = -3\lambda_3. \quad (15)$$

This measure has not been extensively used before and is employed along with  $F$  for the data collected in the ASL and CSL.

### C. Scale-wise analysis

The scale-wise analysis of AIM and BAM uses the structure function approach (in physical or  $r$ -space) instead of Fourier space. The overall premise is similar to what was proposed earlier [28] except that structure functions ensure integrability and minimize other limitations discussed elsewhere for spectral and co-spectral versions [23]. The premise of the scale-wise AIM or BAM analysis is to replace  $\overline{u_i u_j}$  by

$$D_{ij}(r) = \frac{1}{2} \overline{\Delta u_i(r) \Delta u_j(r)}, \quad (16)$$

where  $\Delta u_k(r) = u_k(x+r) - u_k(x)$ , and  $r$  is the separation distance along the longitudinal (or  $x_1$ ) direction determined from time increments and Taylor's frozen turbulence hypothesis [42, 43] as conventional when interpreting time series in field experiments. Equation 16 has a number of desirable limits. To illustrate, consider its expansion given as

$$D_{ij}(r) = \frac{1}{2} \left( \overline{u_i(x+r)u_j(x+r)} + \overline{u_i(x)u_j(x)} \right) + \frac{1}{2} \left( \overline{u_i(x+r)u_j(x)} + \overline{u_i(x)u_j(x+r)} \right). \quad (17)$$

For planar homogeneous flows and at  $r/L_I \gg 1$ ,  $D_{ij}(r) \approx \overline{u_i(x)u_j(x)}$  (or  $D_{ij}(r) \approx \overline{u_i(x+r)u_j(x+r)}$ ), where  $L_I$  is the integral length scale of the flow (to be defined later). Hence,  $D_{ij}(r)$  recovers all the properties of the stress tensor at large-scales. For  $r \rightarrow 0$ ,  $D_{ij}(r) \rightarrow 0$  and ensures no energy and stress contributions at very small scales. The use of  $D_{ij}(r)$  is rather convenient because expected scaling laws for inertial subrange eddies are known. For example, when  $i = 1$  and  $j = 1$ ,  $D_{11}(r)$  becomes the longitudinal velocity structure function, which measures the integrated energy content at scale  $r$ . It is noted here that  $rdD_{11}(r)/dr \propto k_1 E_{11}(k_1)$ , where  $k_1$  is the one-dimensional wavenumber along direction  $x_1$  and  $E_{11}(k_1)$  is the longitudinal velocity energy spectrum. Likewise, for  $r/L_I \gg 1$ ,  $D_{11}(r) \rightarrow \overline{u_1 u_1}$ . Because structure functions measure integrated energy content at a given scale  $r$ , the singularity issues in Fourier domain noted elsewhere [23] are by-passed. For locally isotropic turbulence and for  $\eta/L_I \ll r/L_I \ll 1$ , Kolmogorov (or K41) scaling is expected to hold in the ASL and yields the following for the component-wise structure functions:

$$D_{11}(r) = C_{o,1} \bar{\epsilon}^{2/3} r^{2/3} \quad (18)$$

$$D_{22}(r) = C_{o,2} \bar{\epsilon}^{2/3} r^{2/3} \quad (19)$$

$$D_{33}(r) = C_{o,3} \bar{\epsilon}^{2/3} r^{2/3}, \quad (20)$$

where  $\eta = (\nu^3/\bar{\epsilon})^{1/4}$  is the Kolmogorov microscale,  $\nu$  is the fluid kinematic viscosity,  $C_{o,2} = C_{o,3} = (4/3)C_{o,1}$ ,  $C_{o,1} = 2$ , and  $\bar{\epsilon}$  is the mean dissipation rate of  $k$ . One undesirable outcome to using  $D_{ij}(r)$  is its non-zero trace

at any  $r$ . As was the case with  $a_{ij}$  and  $\overline{u_i(x)u_j(x)}$ , this outcome may be circumvented by evaluating

$$A_{ij}(r) = \frac{D_{ij}(r)}{D_{kk}(r)} - \frac{1}{3} \delta_{ij}. \quad (21)$$

The AIM and BAM as well as  $F(r)$  and  $C_{ani}(r)$  can now be computed for the ASL and CSL velocity time series once the eigenvalues of  $D_{ij}(r)$  or  $A_{ij}(r)$  are determined for each  $r > 0$ .

### D. Comparison with a reference model

To compare the computed scale-wise variations of  $I_2$  and  $I_3$  in the CSL and ASL with a well-studied turbulent state, the homogeneous turbulence (i.e. lacking any mean flow gradients) is selected as a reference. Once the mean flow gradients are removed for this reference state, the decay rates of  $I_2$  and  $I_3$  are shown to reasonably follow a quadratic model given by [27]

$$\frac{dI_2}{d\tau} = -2(B_1 - 2)I_2 + 2B_2 I_3 \quad (22)$$

$$\frac{dI_3}{d\tau} = -3(B_1 - 2)I_3 + \frac{1}{2}B_2 I_2^2, \quad (23)$$

where  $\tau$  is a relaxation time scale, and  $B_1 = 3.4$  and  $B_2 = 3(B_1 - 2)$  are constants determined by fitting this model to a wide range of experiments. For  $B_2 = 0$ , this system recovers the Lumley model [33] (i.e. uncoupled equations), and for  $B_2 = 0$  and  $I_3 = 0$ , the classical Rotta model is recovered. Hence, finite  $B_2$  and  $I_3$  offer a clear indication that the linear Rotta model may not be adequate to describe the trajectory towards isotropy. The two ordinary differential equations can now be combined to yield

$$\frac{dI_2}{dI_3} = \frac{-2(B_1 - 2)I_2 + 2B_2 I_3}{-3(B_1 - 2)I_3 + \frac{1}{2}B_2 I_2^2}, \quad (24)$$

which can be solved to yield  $-I_2$  as a function of  $I_3$  (i.e. the trajectory on the AIM) without requiring the determination of time  $\tau$  provided  $\tau$  is sufficiently large to attain the isotropic state. The trajectories of this model (in AIM or BAM) are simply computed here to illustrate how homogeneous turbulence relaxes to the isotropic state once the mean flow gradients (that are prevalent in ASL and CSL) are suppressed. The initial conditions to equation 24 are the measured  $I_2$  and  $I_3$  in the CSL or ASL as determined for  $r/L_I \gg 1$ .

## III. EXPERIMENTS

### A. Research site

The experiments were conducted at the Yatir Forest in southern Israel, which is a planted evergreen pine forest surrounded by a sparse desert like shrubland [44].



The trees were planted in the late 1960s and now cover an approximate area of 28 km<sup>2</sup> [44]. The primary tree species of the forest is *Pinus halepensis* and the shrubland has scattered herbaceous annuals and perennials (mainly *Sarcopoterium spinosum*). The albedo of the forest is low (=12.5%) when compared to the shrubland (=33.7%). In the absence of latent heat fluxes (as is the case in the extensive dry season), this albedo contrast leads to sensible heat fluxes up to 800 W m<sup>-2</sup> during the day over the forest, which can be twice as high as those of the surrounding shrubland [45]. The higher roughness length of the forest also creates friction velocities ( $u_*$ ) of up to 0.8 m s<sup>-1</sup>, which are twice as high as those above the shrubland [45]. These sensible heat flux and friction velocity differences between the forest and shrubland do impact the generation of  $k$ . To illustrate, a stationary and planar-homogeneous flow at high Reynolds number in the absence of subsidence is considered. The  $k$  budget for such an idealized flow is

$$\frac{\partial k}{\partial t} = 0 = -\overline{u_1 u_3} \frac{dU}{dz} + \beta_o g \overline{u_3 T'} + P_D + T_T - \bar{\epsilon}, \quad (25)$$

where  $t$  is time, and the five terms on the right-hand side of equation 25 are mechanical production, buoyant production (or destruction), pressure transport, turbulent transport of  $k$ , and viscous dissipation of  $k$ , respectively,  $\beta_o$  is the thermal expansion coefficient for air ( $\beta_o = 1/T$ ,  $T$  is mean air temperature and  $T'$  is temperature fluctuation),  $g$  is the gravitational acceleration,  $-\overline{u_1 u_3} = u_*^2$  is the turbulent kinematic shear stress near the surface,  $\overline{u_3 T'}$  is the kinematic sensible heat flux from (or to) the surface, and  $U$  is the mean longitudinal velocity. The  $\rho_a C_p \overline{u_3 T'}$  defines the sensible heat flux in energy units (W m<sup>-2</sup>), with  $\rho_a$  and  $C_p$  being the mean air density and the specific heat capacity of dry air at constant pressure, respectively. When  $\overline{u_3 T'} > 0$ , buoyancy is responsible for the generation of  $k$  and the flow is classified as unstable. When  $\overline{u_3 T'} < 0$ , the flow is classified as stable and buoyancy acts to diminish the mechanical production of  $k$ . The relative significance of the mechanical production to the buoyancy generation (or destruction) in the TKE budget may be expressed as [10, 13, 14]

$$-\overline{u_1 u_3} \frac{dU}{dz} + \beta_o g \overline{u_3 T'} = \frac{u_*^3}{\kappa z} \left[ \phi_m(\zeta) + \frac{\kappa z \beta_o g \overline{u_3 T'}}{u_*^3} \right] = \frac{u_*^3}{\kappa z} [\phi_m(\zeta) - \zeta], \quad (26)$$

where

$$\frac{\kappa z}{u_*} \frac{dU}{dz} = \phi_m(\zeta), \zeta = \frac{z}{L}, L = -\frac{u_*^3}{\kappa g \beta_o \overline{u_3 T'}}, \quad (27)$$

and  $\phi_m(\zeta)$  is known as a stability correction function reflecting the effects of thermal stratification on the mean velocity gradient ( $\phi_m(0) = 1$  recovers the von Karman-Prandtl log-law),  $\kappa \approx 0.4$  is the von Karman constant, and  $L$  is known as the Obukhov length [46] as described by the Monin and Obukhov similarity theory [1, 2, 7, 9].

The physical interpretation of  $L$  is that it is the height at which mechanical production balances the buoyant production or destruction when  $\phi_m(\zeta)$  does not deviate appreciably from unity. For a neutrally stratified atmospheric flow,  $|L| \rightarrow \infty$  and  $|\zeta| \rightarrow 0$ . The sign of  $L$  reflects the direction of the heat flux, with negative values of  $L$  corresponding to upward heat fluxes (unstable atmospheric conditions) and positive values  $L$  corresponding to downward heat flux (stable atmosphere).

## B. Instruments and measurements

High frequency measurements of the turbulent velocity components were conducted concurrently in the CSL over the forest and the ASL of the surrounding shrubland desert ecosystem. The measurements in the ASL were conducted northwest of the forest above the shrubland with a mobile mast positioned at latitude 31.3757°, longitude 35.0242°, and 620 m above sea level. The mast was equipped with a R3-100 ultrasonic anemometer from Gill Instruments Ltd (Lymington, Hampshire, UK) sampling three orthogonal velocity components with a frequency of 20 Hz. The ultrasonic anemometer was mounted at a height of 9 m above ground surface. The measurements in the CSL were conducted above the forest canopy with a R3-50 ultrasonic anemometer from Gill Instruments with a measurement frequency of 20 Hz (latitude 31.3453°, longitude 35.0522°, 660 m above sea level). The manufacturer states for both ultrasonic anemometers an accuracy < 1% for mean wind speeds below 32 m s<sup>-1</sup>. Wind tunnel and atmospheric comparison to a hot-film anemometers showed an accuracy of 2% for the mean wind speed, 9% for variances, and 23% for covariances [47]. The sonic anemometer was mounted 19 m above the ground surface on a meteorological tower. The mean height of the trees around the tower is 10 m placing the sonic anemometer some 9 m above the canopy top and commensurate to the setup of the urban roughness study previously discussed [26]. The anemometer sonic path-length is 0.15 m; hence, separation distances smaller than 0.3 m are not used as they are influenced by instrument averaging. Data from the period 17 - 23 August 2015 is used here. During this period, the Yatir forest experienced a subtropical ridge, an area of general subsidence in the troposphere connected to the sinking branch of the Hadley-cell [48]. The horizontal air pressure gradients were controlled by a heat-induced surface low, the Persian trough, to the east [49]. This led to stationary weather conditions with a main wind direction from north-west and cloud free conditions with a radiation driven diurnal cycle of the boundary layer height during the campaign.

### C. Post-processing

The measured  $u_i$  time series were first separated into non-overlapping 30-minute runs, and turbulent flow statistics were computed using the 30-minute averaging period per run. A threshold filter of  $50 \text{ m s}^{-1}$  for the horizontal wind components and  $10 \text{ m s}^{-1}$  for the vertical component was applied and spikes were removed by a five standard deviation threshold. Then gaps in the time series were linearly interpolated when the total gap length was less than 5% (otherwise the 30-minute run was discarded). The interpolated data set was rotated into the mean wind direction using a standard double rotation ( $\overline{u_3} = \overline{u_2} = 0$  and  $U \neq 0$ ) and the mean value was subtracted to obtain turbulent fluctuations. Further quality control was conducted using stationary tests and integral turbulence characteristic tests described elsewhere [50], and only intervals with the best quality metrics were used [51]. For comparison purposes, only intervals where both sites had simultaneous high quality measurements were used. After such post-processing, 65 runs remained for investigating the anisotropy in the ASL and CSL.

## IV. RESULTS AND DISCUSSION

To address the study objective, the results are presented as follows: the  $a_{ij}$  components computed from equation 1 for the ASL and CSL and their dependence on  $\zeta$  are first presented. Similarities between anisotropy in component-wise turbulent kinetic energy and integral scales along the  $x_1, x_2, x_3$  are also featured. Next, attainment of local isotropy at finer scales is explored by comparing measured  $D_{11}(r)$ ,  $D_{22}(r)$ , and  $D_{33}(r)$  with predictions from K41 scaling and corollary isotropic measures. The scale-wise development of the anisotropic stress tensor ( $A_{ij}(r)$ ) for the ASL and CSL, as determined from equation 21, is then discussed using AIM and BAM. Predictions from equation 24 are displayed as reference to illustrate expected pathways by which  $A_{ij}(r)$  approaches its isotropic state with decreasing  $r$  for homogeneous turbulence. Finally, the two scale-wise measures  $F(r)$  and  $C_{ani}(r)$  are presented as a function of  $r$  for CSL and ASL flows across a wide range of  $\zeta$  values. The focus here is on two types of scales: (i) the largest  $r$  for which local isotropy is attained, and (ii) the smallest  $r$  over which the return-to-isotropy begins to be efficient. These two scales are then contrasted for ASL and CSL flows and across  $\zeta$  values thereby completing the sought objective.

### A. Conventional Analysis

Unsurprisingly, the computed  $a_{ij}$  components exhibit large anisotropy for both ASL and CSL flows. In particular, the streamwise  $a_{11}$  and the cross-streamwise  $a_{22}$  attain positive values (i.e. more energy than isotropic

predictions) as evidenced by Fig. 1a and 1b and negative values for the vertical  $a_{33}$  (Fig. 1c) when compared to the expected  $Y = 0$  designating isotropic state. The streamwise and cross-stream components show that the anisotropy for near neutral conditions in the CSL is between the vertical and streamwise components. The sum of the two horizontal components ( $a_{11} + a_{22} = -a_{33}$ ), which accounts for much of the  $k$ , is expected to provide a robust measure of the anisotropy between the horizontal and vertical components. The mean values for  $a_{33}$  differ between CSL and ASL at a 95% confidence level confirming a significantly larger anisotropy in the ASL when compared to its CSL counterpart. The analysis here also shows that  $a_{33}$ , and  $a_{23}$  are not sensitive to variations in  $\zeta$  for both ASL and CSL flows. The only component of  $a_{ij}$  that exhibits variation with  $\zeta$  is  $a_{13}$  in the CSL, which has a slope significantly different from zero at a 95% confidence level. The  $a_{13}$  is small in the ASL by comparison to its CSL values. The scatter of most data points in Fig. 1 can be explained by the measurement accuracy, but in case of  $a_{11}$  and  $a_{22}$  the accuracy alone cannot explain the variation and it is likely that non-stationary wind directions affect those components. Direct numerical simulations of homogeneous turbulent shear flows showed more isotropy for weaker shear [52], which agrees with experiments here where the CSL appears more isotropic and has weaker shear parameter  $S^*$  compared to its ASL counterpart for near-neutral conditions. Moreover, the simulation results [52] showed similar patterns among the components of  $a_{ij}$  as the atmospheric measurements reported in Figure 1 for a near-neutral ASL. The  $S^*$  here varied from 35 – 83 compared to their highest  $S^* = 27$ , where  $S^* = Sk^2/\epsilon$  with  $S = U/(z - d)$ . Moreover, these simulations do not have a 'wall' thereby suppressing any possible wall-blocking likely to be higher in the ASL than the CSL. As earlier noted, the  $u_*^2$  is larger for the CSL when compared to the ASL due to the rougher forest cover. While  $\overline{u_3 u_3}/u_*^2$  increases with increasing  $-\zeta$ ,  $\overline{u_1 u_1}/u_*^2$  and  $\overline{u_2 u_2}/u_*^2$  vary with both  $-\zeta$  and  $\log(z/h_{BL})$ , where  $h_{BL}$  is the boundary layer height as discussed elsewhere [16, 17, 53–55] with higher values (and fraction of  $k$ ) in the ASL when compared to the CSL. Separate field experiments suggest that  $h_{BL}$  above the forest and the shrubland are comparable [56] (and by design, so are the  $z$  values in the CSL and ASL). These findings explain the lower measured  $k/u_*^2$  in the CSL (Fig. 1f) when compared to its ASL counterpart given the larger  $u_*$  over the forest. While  $\overline{u_1 u_1}/u_*^2$ ,  $\overline{u_2 u_2}/u_*^2$  and  $\overline{u_3 u_3}/u_*^2$  follow expectations for near-neutral conditions from a mixing layer analogy [5] in the CSL, these flow statistics were higher than expected for the ASL (not shown). A plausible explanation for higher than expected values in the ASL are some topographic variability upwind of the ASL measurement tower. However, the aforementioned topographic variability did not affect the anisotropy appreciably given that canopy sublayer experiments (field and laboratory) collected at  $z/h=1$  yield  $\sigma_{u3}(\sigma_{u1} + \sigma_{u2})^{-1} = 0.30$  (with

433  $\sigma_{ui} = \sqrt{u_i u_i}$  whereas surface layer experiments yield  
 434  $\sigma_{u3}(\sigma_{u1} + \sigma_{u2})^{-1} = 0.25$  to which ASL and CSL appear  
 435 to be commensurate for near-neutral conditions (Fig. 1g).  
 436 To contrast energy anisotropy with eddy size  
 437 anisotropy along the  $x_1$ ,  $x_2$ , and  $x_3$  directions, the effective  
 438 eddy sizes for the  $u_i$  are determined from the integral  
 439 time scale  $I_{ui}$  and Taylor's frozen turbulence hypothesis  
 440 [42] using

$$L_{ui} = U \cdot I_{ui} = U \cdot \int_0^\infty \rho_{ui}(\tau_0) d\tau_0, \quad (28)$$

441 where  $\rho_{ui}(\tau_0)$  is the  $u_i$  velocity component autocorrela-  
 442 tion function and  $\tau_0$  is the time lag. Here,  $L_{u3}$  is pre-  
 443 sumed to be the most restrictive scale given that  $u_3$  is  
 444 the flow variable most impacted by the presence of a  
 445 boundary (porous in the CSL and solid in the ASL). The  
 446 calculations show that  $L_{u3}/z$  is on the order of unity  
 447 for the CSL but higher in the ASL for near-neutral con-  
 448 ditions (Fig. 2a). As expected,  $L_{u3}/L_{u1}$  (Fig. 2b) and  
 449  $L_{u3}/L_{u2}$  (Fig. 2c) are well below unity for both ASL and  
 450 CSL flows and do not vary appreciably with  $\zeta$ . Roughly,  
 451  $L_{u1}$  is about a factor of 10 larger than  $L_{u3}$  (shown as  
 452 dashed line) in agreement with prior CSL [57] and ASL  
 453 [58] experiments. Interestingly, the shape of the normal-  
 454 ized energy distribution ellipsoid observed in Fig. 1 is  
 455 qualitatively similar to the effective eddy sizes but they  
 456 are not identical. Because  $L_{u3}$  is the most restrictive  
 457 eddy size and partly captures some effects of  $\zeta$  on elonga-  
 458 tion or compression of eddy sizes (Fig. 2a), the scale-wise  
 459 analysis is to be reported as  $r/L_{u3}$  (instead of  $r/z$ ) for  
 460 each run. It is also worth noting that  $r/L_{u3}$  may be in-  
 461 terpreted as normalized time-scale separation given that  
 462 Taylor's hypothesis equally impacts the numerator and  
 463 denominator. While Taylor's hypothesis is not expected  
 464 to be suitable near roughness elements [59] in the CSL,  
 465 its distortions become less severe beyond  $z/h > 2$ , the  
 466 case for the CSL here.

467 The ensemble-averaged (over  $\zeta$ ) normalized  
 468  $D_{11}/\overline{2u_1u_1}$ ,  $D_{22}/\overline{2u_2u_2}$ , and  $D_{33}/\overline{2u_3u_3}$  approaches  
 469 unity at large  $rL_{u3}^{-1}$  consistent with expectations from  
 470 stationarity arguments (Fig. 3). However, stationarity  
 471 appears to be attained at smaller  $rL_{u3}^{-1}$  for the CSL  
 472 when compared to its ASL counterpart. The fact  
 473 that  $D_{11}/\overline{2u_1u_1}$  exhibits an approximate logarithmic  
 474 region at scales larger than inertial but smaller than  
 475 scales where  $dD_{11}(r)/dr \approx 0$  is not surprising for the  
 476 ASL and is consistent with prior theoretical analysis  
 477 explaining the  $-1$  power-law in the longitudinal ve-  
 478 locity spectrum at large-scales as well as laboratory  
 479 studies, field experiments, and Large Eddy Simulations  
 480 [55, 60–68]. Such logarithmic transition between inertial  
 481 and  $dD_{11}(r)/dr \approx 0$  is much more restricted in scale  
 482 separation within the CSL.

483 At about  $r/L_{u3} = 1/2$ , all velocity component struc-  
 484 ture functions follow the  $r^{2/3}$  K41 scaling consistent  
 485 with other ASL experiments [69, 70]. However, second-  
 486 order structure function scaling-laws are only a necessary  
 487 but not sufficient condition to the attainment of local

isotropy. The component-wise velocity structure function  
 ratios against  $r/L_{u3}$  demonstrate that anisotropy exists  
 at fine scales even for  $r/L_{u3} = 1/2$  and for both - ASL  
 and CSL flows (Fig. 4). However, for  $r/L_{u3} < 0.1$ , predic-  
 tions from local isotropy agree with measurements. The  
 calculations were repeated for  $D_{11}/D_{33}$  and  $D_{22}/D_{33}$  to  
 correct for finite squared turbulent intensity effects us-  
 ing the linear model of Wyngaard and Clifford (1977)  
 [43, 71]. The results do not deviate appreciably from di-  
 rect application of Taylor's frozen turbulence hypothesis  
 assuming small turbulent intensity (figure not shown). It  
 is precisely the nature of this anisotropy that we seek to  
 address using the invariance measures across scales.

## 501 B. Invariant Analysis

502 The return-to-isotropy trajectories are shown in BAM  
 503 for all ensemble members (Fig 5a and 5b). The starting  
 504 and end points of the scale-wise trajectories are consis-  
 505 tent with the conventional analysis previously discussed:  
 506 large scales are further away from the isotropic (or 3D)  
 507 limit for the ASL when compared to the CSL. The  $\zeta$  vari-  
 508 ations also show no significant influence on the starting  
 509 position of the points within the BAM (Fig. 5a and 5b).

510 The relaxation trajectories towards isotropic (or 3D)  
 511 state with decreasing scale  $r$  appears to be shorter for  
 512 the CSL when compared to the ASL. Trajectories, by  
 513 and large, show a return-to-isotropy by a contraction in  
 514 the proximity of the 2D-3D limit for near-neutral and  
 515 unstable  $\zeta$ . However, the trajectory for stable condi-  
 516 tions is closer to the center of the BAM (Fig. 5c and  
 517 5d). In all cases, meandering of trajectories in the BAM  
 518 with decreasing scale deviate from predictions based on  
 519 zero-mean shear or homogeneous turbulence. These de-  
 520 viations partly reflect contributions from  $dU/dz$  that is  
 521 active on all scales. In the AIM, the trajectories show  
 522 rough similarities in curvature to the model for homo-  
 523 geneous turbulence (Eq. 24) at the same starting posi-  
 524 tion. This agreement is mainly due to the compressed  
 525 trajectory representation of AIM near the isotropic limit  
 526 corner as discussed elsewhere [32]. The deviation be-  
 527 tween modeled and measured trajectories is quantified  
 528 as the shortest distance in the BAM for a given  $r$  by  
 529  $d(dI_2/dI_3, \vec{n}_{BAM})$  with  $\vec{n}_{BAM} = (x_{BAM}, y_{BAM})$  given  
 530 by Eq. 12 and  $dI_2/dI_3$  by Eq. 24. The ensemble av-  
 531 erage of the deviation is decreasing towards the large  
 532 scales, because we initialized the model with the mea-  
 533 surements at the starting point of the trajectory, and  
 534 at small scales where both converge to isotropic state  
 535 (Fig. 5e and 5f). In between the return-to-isotropy of the  
 536 Rotta model shows significant deviations from the mea-  
 537 surements, which cannot be explained by the measure-  
 538 ment errors. The measurement errors were computed em-  
 539 pirically by generating 2500 realizations of the anisotropy  
 540 tensor  $a_{ij}$  from the accuracy of the covariance assuming  
 541 a normal distribution. Each  $a_{ij}$  was then diagonalized to  
 542 gain a distribution of the eigenvalues and subsequently



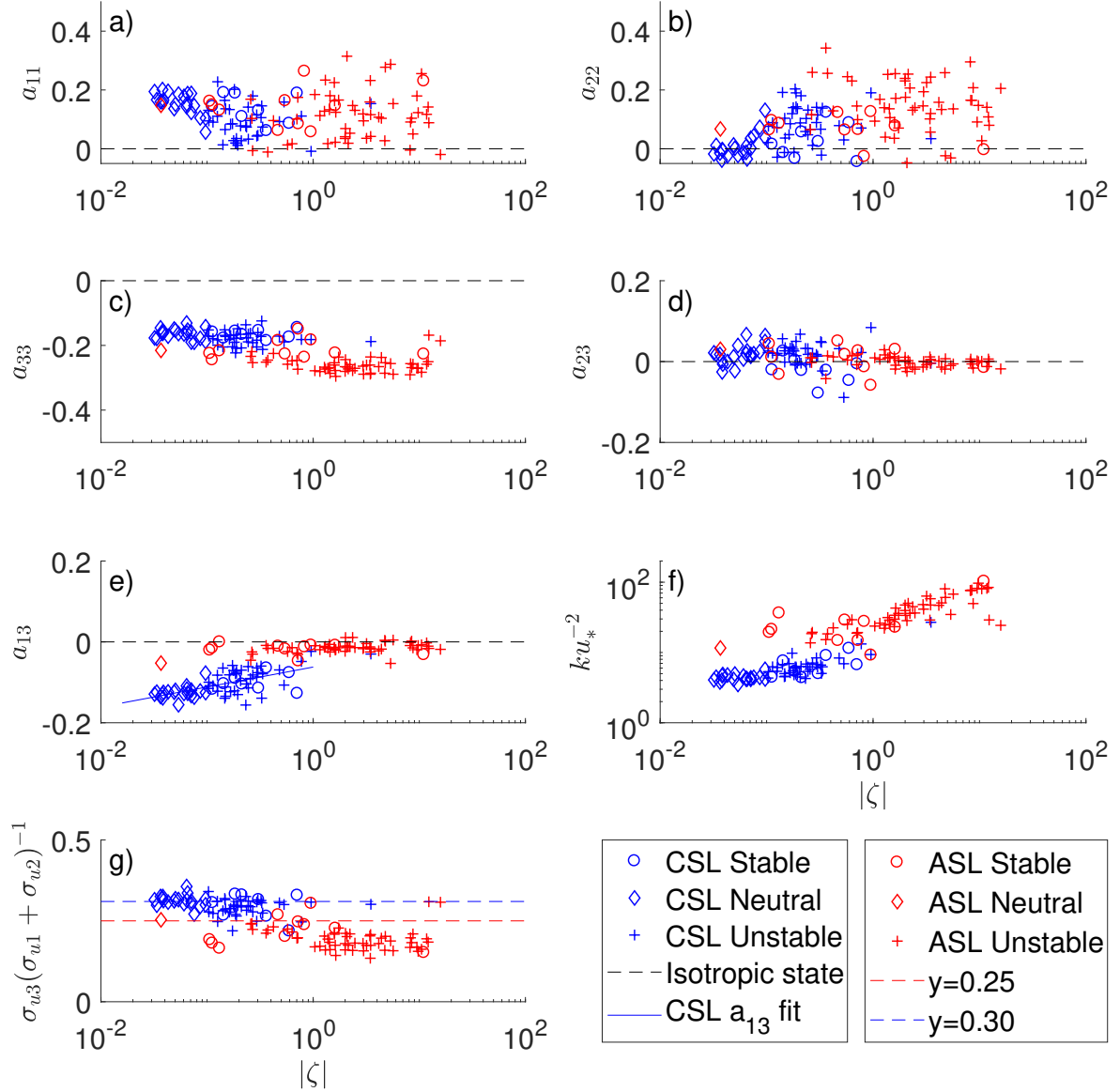


FIG. 1. The measured components of the anisotropy tensor  $a_{ij}$  are shown as a function of the absolute value of the stability parameter  $|\zeta| = |(z - d)/L|$  (a, b, c, e). Measurements of the ASL (desert) are red and of the CSL (forest) are blue. Circles show stable conditions, diamonds are used for near neutral stratification conditions and crosses for unstable conditions. The  $a_{33}$  shown in panel c) are significantly larger in the CSL compared to the ASL at a confidence level of 95%. The black dashed line shows the expected value for isotropic turbulence and the solid blue line in panel e) shows a linear regression of  $a_{33}$  for the CSL. The lower right panel (f) shows turbulent kinetic energy  $k$  normalized with  $u_*$  and the lower left panel (g) shows  $\sigma_{u3}(\sigma_{u1} + \sigma_{u2})^{-1}$  together with the expectation for near neutral conditions as dashed lines [5]. Note the larger  $\sigma_{u3}(\sigma_{u1} + \sigma_{u2})^{-1}$  for the CSL when compared to the ASL.

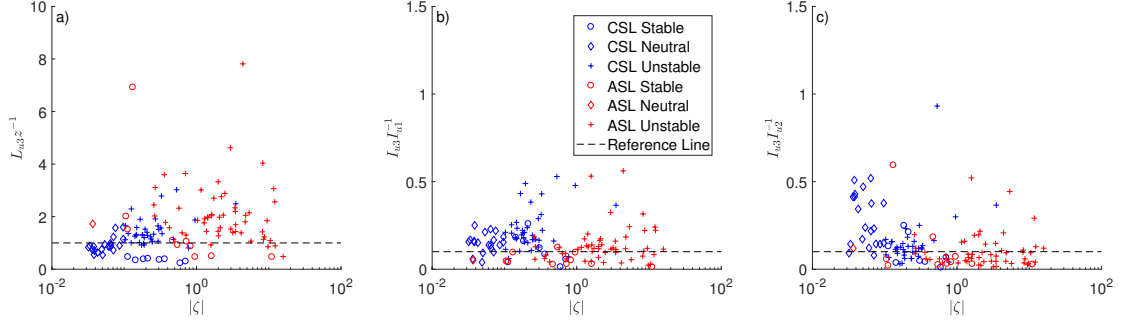


FIG. 2. Normalized length scale  $L_{u3}z^{-1}$  (a) and the length scale ratios  $L_{u3}L_{u1}^{-1}$  (b) and  $L_{u3}L_{u2}^{-1}$  (c) are shown as a function of the absolute value of the stability parameter  $|\zeta| = |(z - d)/L|$ . Measurements of the ASL (desert) are red and of the CSL (forest) are blue. Unstable stratification is shown as crosses, near neutral as diamonds and stable as circles. The dashed line in panels (b) and (c) shows  $L_{u3}L_{u1}^{-1} = 0.1$  reported from other experiments [57, 58].

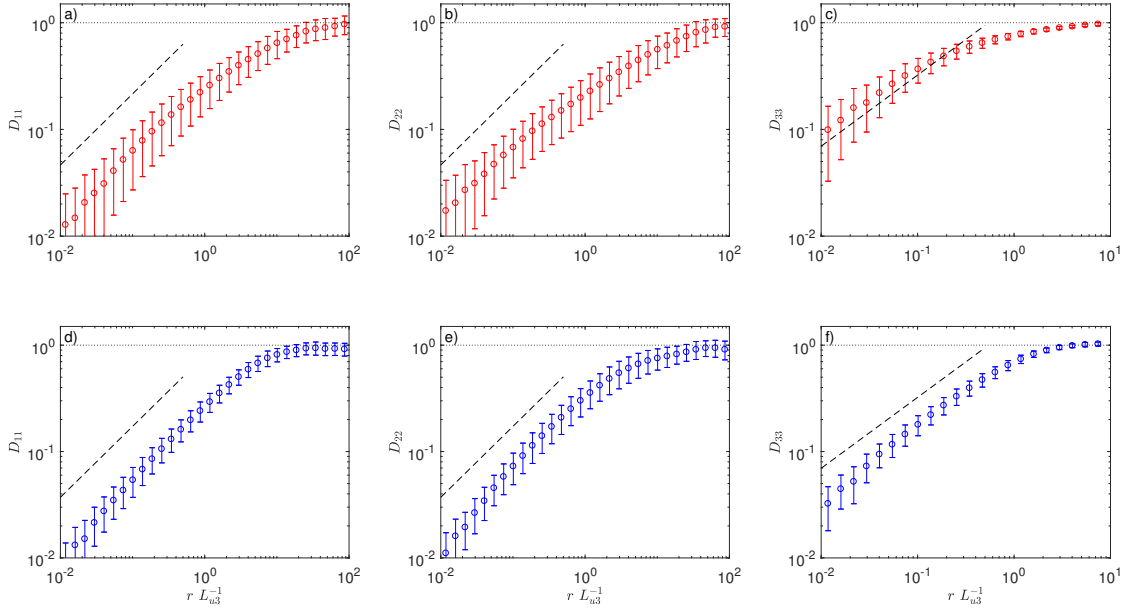


FIG. 3. Ensemble averaged of normalized structure function  $\frac{1}{2}D_{11}\overline{u_1u_1}^{-1}$  (left column),  $\frac{1}{2}D_{22}\overline{u_2u_2}^{-1}$  (middle column) and  $\frac{1}{2}D_{33}\overline{u_3u_3}^{-1}$  (right column) are shown for the ASL (top, red) and CSL (bottom, blue). The black dotted line is  $y = 1$  and the black dashed line shows the slope  $r^{2/3}$  for Kolmogorov scaling (Eq. 18). The error bars show the standard deviation of the ensemble.

a distribution of  $\vec{n}_{BAM}$ . From this the measurement error is estimated as the standard deviation of the distance between the mean of  $\vec{n}_{BAM}$  (which is equal to measurements) and each ensemble member.

An ensemble average of all runs shows at which  $rL_{u3}^{-1}$  the return to isotropy commences and terminates using both  $F$  and  $C_{iso}$  (Fig. 6). While the  $F$  (or AIM) measure suggests near-isotropic conditions at small scales, the  $C_{iso}$  (or BAM) measure suggests small but sustained anisotropy at those same small scales. As earlier noted, the AIM compresses the trajectories (and distance) near isotropic states, whereas BAM does not. Consistent with

the previous structure function analysis, a near local isotropy at small scales  $rL_{u3}^{-1} < 0.5$  is attained where as anisotropy exists at larger scales. The ASL is shown to be more anisotropic at large scales ( $rL_{u3}^{-1} > 100$ ) when compared to the CSL. Both anisotropy measures reveal three separated regimes: scale independent anisotropy at large scales where  $F$  and  $C_{iso}$  are constantly low but approximately independent of scale (anisotropy is large), a return-to-isotropy regime in which the flow begins to relax towards isotropy as smaller scales are approached, and a third regime where scale independent near-isotropy at small scales is attained (anisotropy is weak). The up-

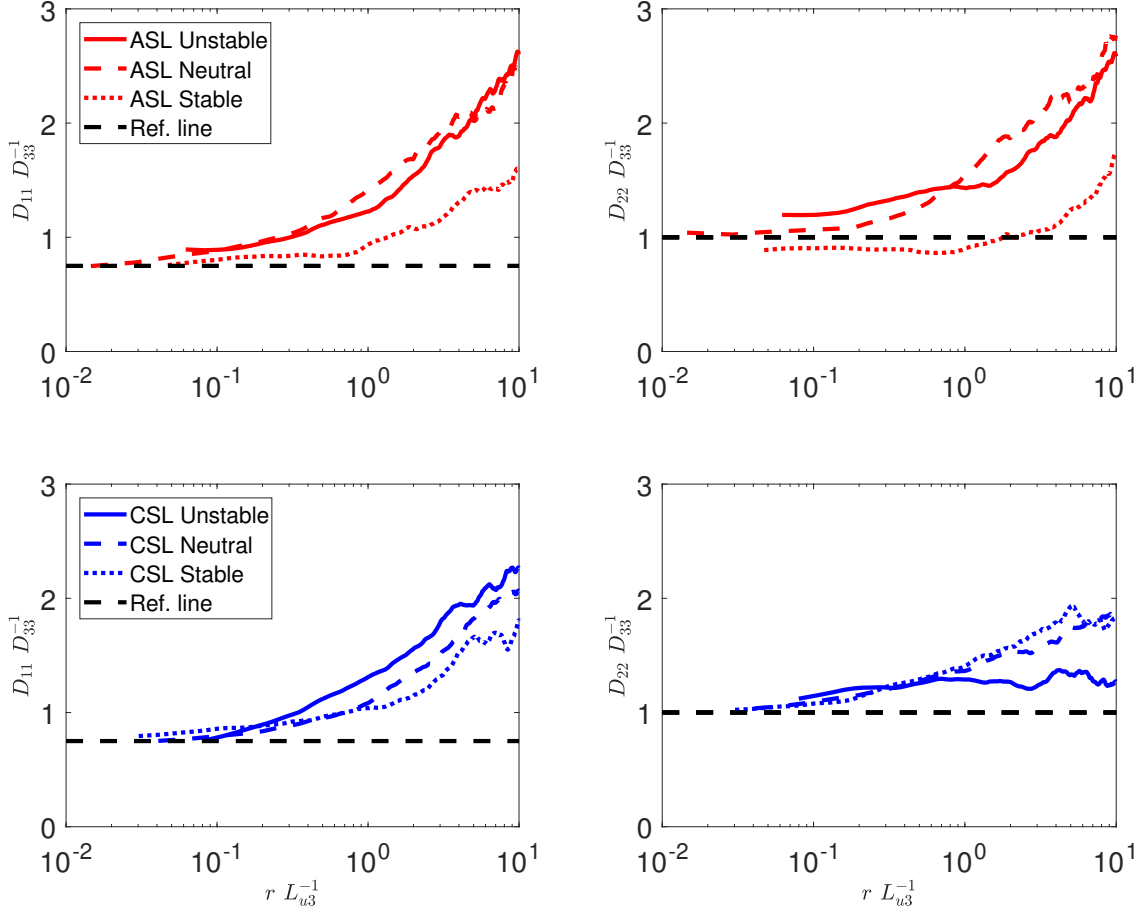


FIG. 4. Local isotropy attained by the ratios  $D_{11}D_{33}^{-1}$  (left column) and  $D_{22}D_{33}^{-1}$  (right column) for the ASL (top row, red) and CSL (bottom row, blue). The three lines show one example interval for stable (solid), neutral (dashed) and unstable (dotted) conditions. The black dashed line shows the expected ratio for locally isotropic turbulence based on K41.

per and lower scales bounding this intermediate regime are hereafter designated as  $r_{ani}$  and  $r_{iso}$ , respectively. They were determined from the scale  $r$  where  $C_{ani}$  has reached 90% of maximum isotropy (approaching from large  $r$ ) in case of  $r_{iso}$  and from the scale  $r$  where  $C_{ani}$  was within 10% of its lowest value (approaching from small  $r$ ) in case of  $r_{ani}$ . In the ASL, the return-to-isotropy is initiated at larger scales ( $r_{ani}L_{u3}^{-1} > 70$ ) when compared to the CSL ( $r_{ani}L_{u3}^{-1} > 25$ ) and covers a wider scale range. The scales at which local isotropy is roughly attained ( $r_{iso}L_{u3}^{-1} = 0.5$ ) are comparable for the ASL and CSL. The experiments above urban canopies suggested that  $r_{ani}$  varies with an outer length scale associated with the peak in the air temperature spectrum [26]. A similar analysis was conducted using the integral length scale of the air temperature time series  $L_{uT}$  and the outcome is featured in Fig. 7. When analyzing all the individual runs,  $r_{ani}$  is smaller for stable than for unstable conditions for the CSL but not the ASL (Fig. 7a). Also,  $r_{ani}$  has a weak dependency on  $L_{uT}$  for the ASL but

not for the CSL (Fig. 7a). In contrast,  $r_{iso}$  is less sensitive to variations in  $L_{uT}$  (Fig. 7b), especially in the ASL ( $r_{iso} \approx z/2$ ). Normalizing  $r_{ani}$  and  $r_{iso}$  with  $L_{u3}$  removes any  $L_{uT}$  dependency in the ASL (Fig. 7c and d) and the correlation coefficient of  $L_{uT}$  and  $r_{ani}$  decreases from 0.43 to 0.02 and in case of  $r_{iso}$  from 0.40 to  $-0.12$  (in the CSL all correlation coefficients are smaller than 0.14). That is, much of the dependency of  $r_{ani}$  on  $L_{uT}$  in the ASL can be attributed to variations in  $L_{u3}$  with  $-\zeta$ . Furthermore, ensemble averages of  $r_{ani}$  are significantly different for CSL and ASL and remain significantly different for flows, but this difference is collapsed if  $r_{iso}$  is normalized with  $L_{u3}$ . These results are robust even when other methods for determining  $r_{ani}$  and  $r_{iso}$  (e.g. fitting a tangent hyperbolic function) are employed (not shown). In comparison to experiments above urban canopies [26], values of  $L_{uT}$  cover similar ranges in the ASL and CSL. The range  $r_{ani}$  covers more than a decade if ASL and CSL

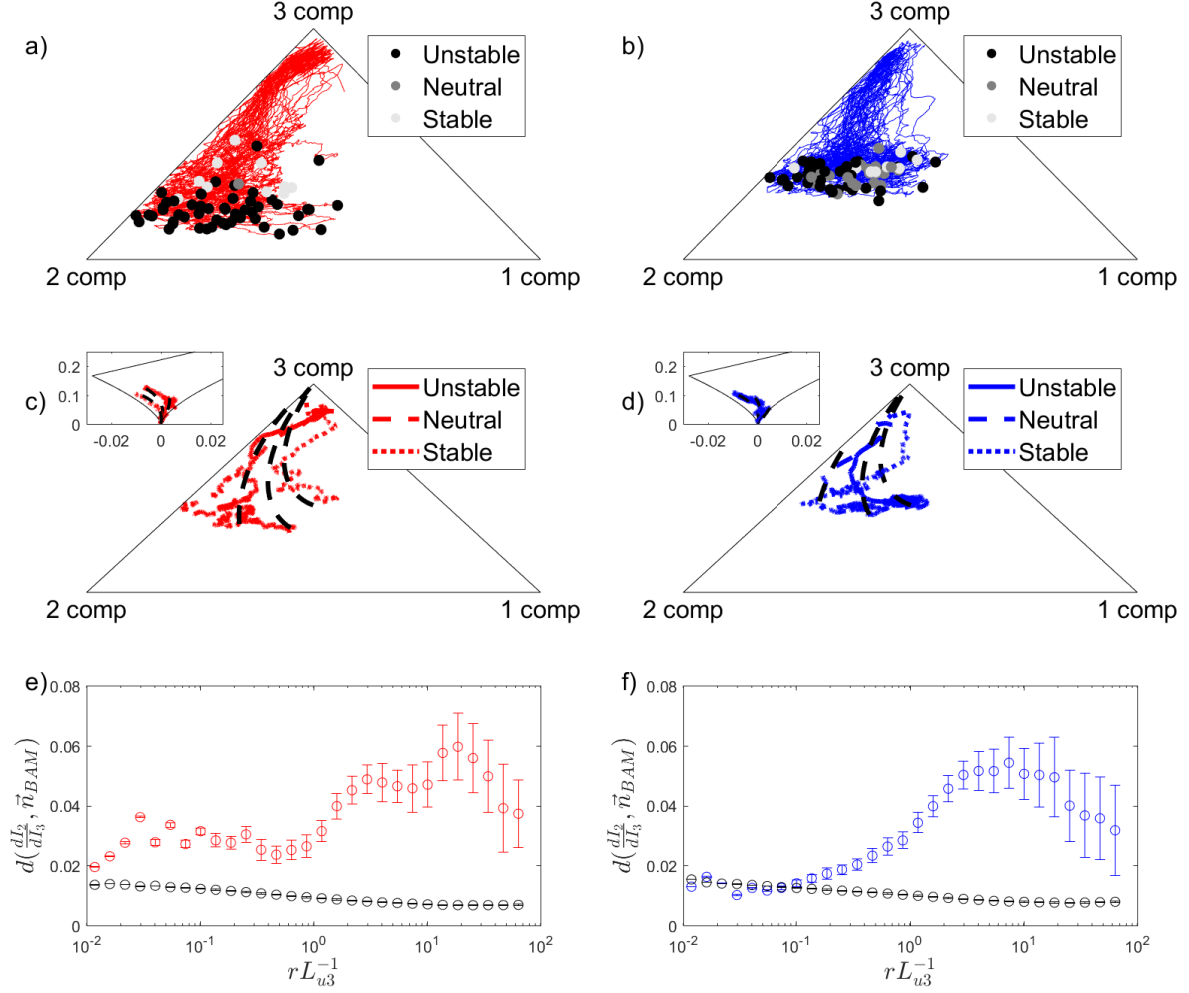


FIG. 5. The top row shows the trajectories of all 30 minute runs for the ASL (a) and the CSL (b) together with starting points color coded according to their stability class (black is unstable, dark grey is near neutral and light grey is stable). The middle row shows return-to-isotropy trajectories in the BAM for three sample cases with unstable, neutral and stable stratification of the ASL (c) and CSL (d) together with model trajectories (Eq. 24). The insets show the same three trajectories in the AIM representation. The bottom row shows the mean distance between modeled and measured trajectories in BAM, with the standard deviation as error bars, for the ASL (e) and CSL (f) together with the part of these deviation, which can be explained by the measurement errors (black).

607 results are treated separately (and when excluding the  
 608 data point with  $r_{ani} = 5$  for the CSL), which is larger  
 609 range than observed above urban canopies. It may be  
 610 surmised that the return-to-isotropy depends more on  
 611 roughness properties and less on surface heating or cool-  
 612 ing for the same  $L$ .

613 The persistence of anisotropy at small scales has been  
 614 extensively studied and linked to the finite mean velocity  
 615 gradient [72, 73]. The so-called integral structure func-

tion of order  $n$ , defined as

$$\left[ \Delta u_k(r)^3 + \alpha_c r \frac{dU}{dz} \Delta u_k(r)^2 \right]^{n/3}, \quad (29)$$

617 has been shown to recover measured structure functions  
 618 in laboratory settings and simulations [72, 73] at small  
 619 scales, where  $\alpha_c$  is a similarity constant. The prevalence  
 620 of  $dU/dz$  acting on all scales suggests that anisotropy pro-  
 621 duced by the mean velocity gradient can persist through-  
 622 out the inertial subrange via finite co-spectra [74, 75].  
 623 This argument was recently suggested to explain persis-  
 624 tent anisotropy in the urban surface layer [26]. In terms



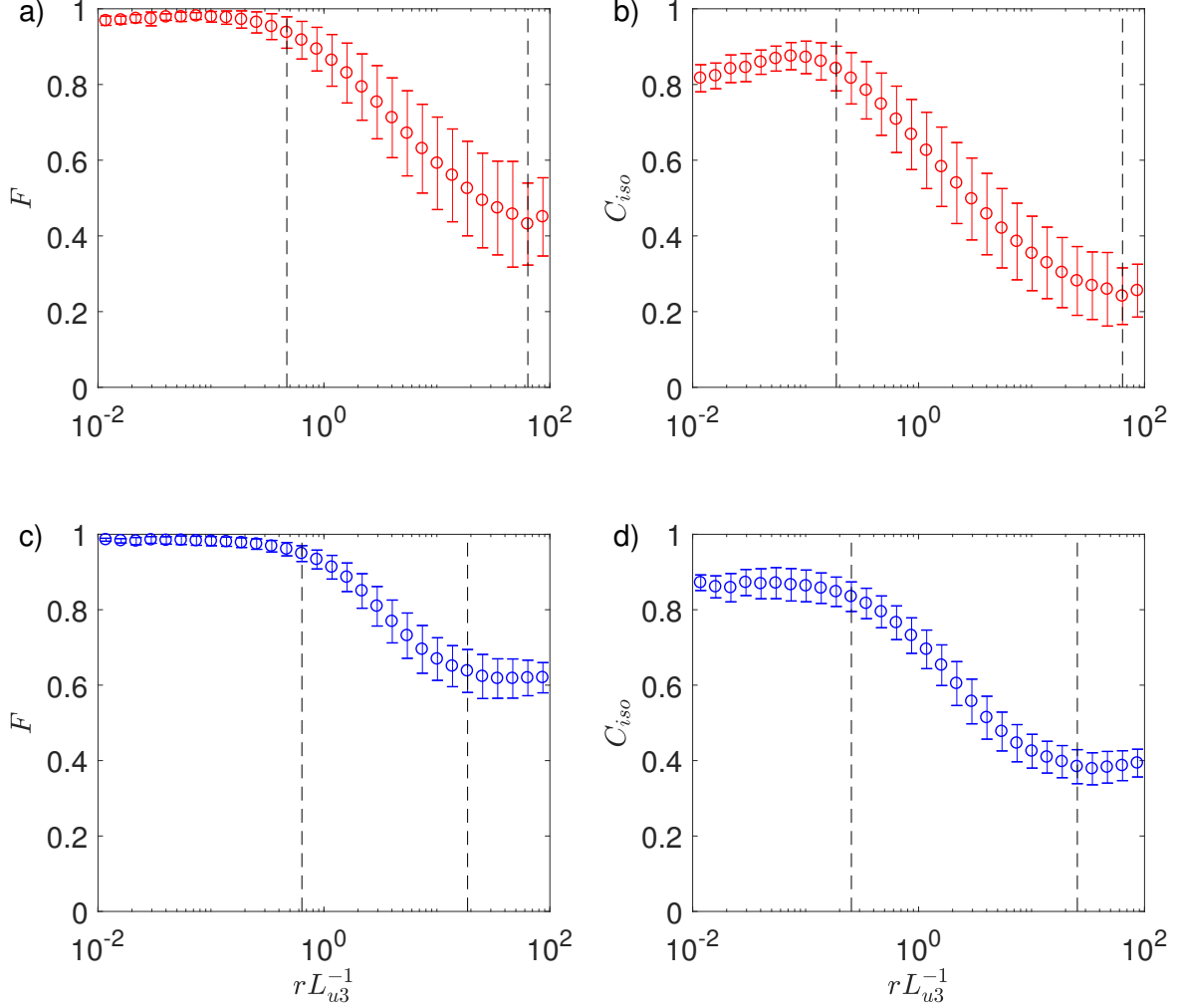


FIG. 6. Anisotropy measures  $F$  (left column, Eq. 14) and  $C_{ani}$  (right column, Eq. 15) are shown for ASL (top row, red) and CSL (bottom row, blue) as ensemble average with standard deviation across all  $\zeta$  to highlight the role of surface roughness. The black dashed lines show three regimes defined by reaching 90% of maximum isotropy or 10% of anisotropy.

of a lower boundary condition on the flow, this mean velocity gradient is linked to the shear stress and thermal stratification by

$$\frac{dU}{dz} = \phi_m(\zeta) \frac{u_*}{\kappa z}. \quad (30)$$

For near-neutral conditions (i.e.  $\phi_m(0) = 1$ ) and at a fixed  $z$ , increasing  $u_*$  increases  $dU/dz$ .

In the case of the CSL,  $u_*$  and  $dU/dz$  are expected to be higher than their ASL counterpart if  $\kappa z$  is similar. However, the invariant analysis here suggests that ASL is more anisotropic at fine scales  $r < r_{iso}$ . Hence, shear intensity (or  $dU/dz$ ) alone cannot be the main cause. The alternative explanation stems from the fact that  $\sigma_{u3}/(\sigma_{u1} + \sigma_{u2})$  is larger for the CSL when compared to its ASL counterpart for similar  $\zeta$  values. While both

ASL and CSL turbulence appear to be isotropic in the plane paralleling the ground surface, the CSL energy ellipsoid appears to be closer to a 3D when compared to its ASL counterpart. This initial energy configuration state at large scales in the ASL requires that the return-to-isotropy transfer more energy to the vertical direction when compared to the CSL.

## V. BROADER IMPACTS

The results presented here are pertinent to subgrid-scale turbulence closure schemes in Large Eddy Simulations. Most models use subgrid-scale stress parametrization based on isotropic eddy-diffusivity schemes (e.g. PALM [76–78]). Turbulence closure methods accounting

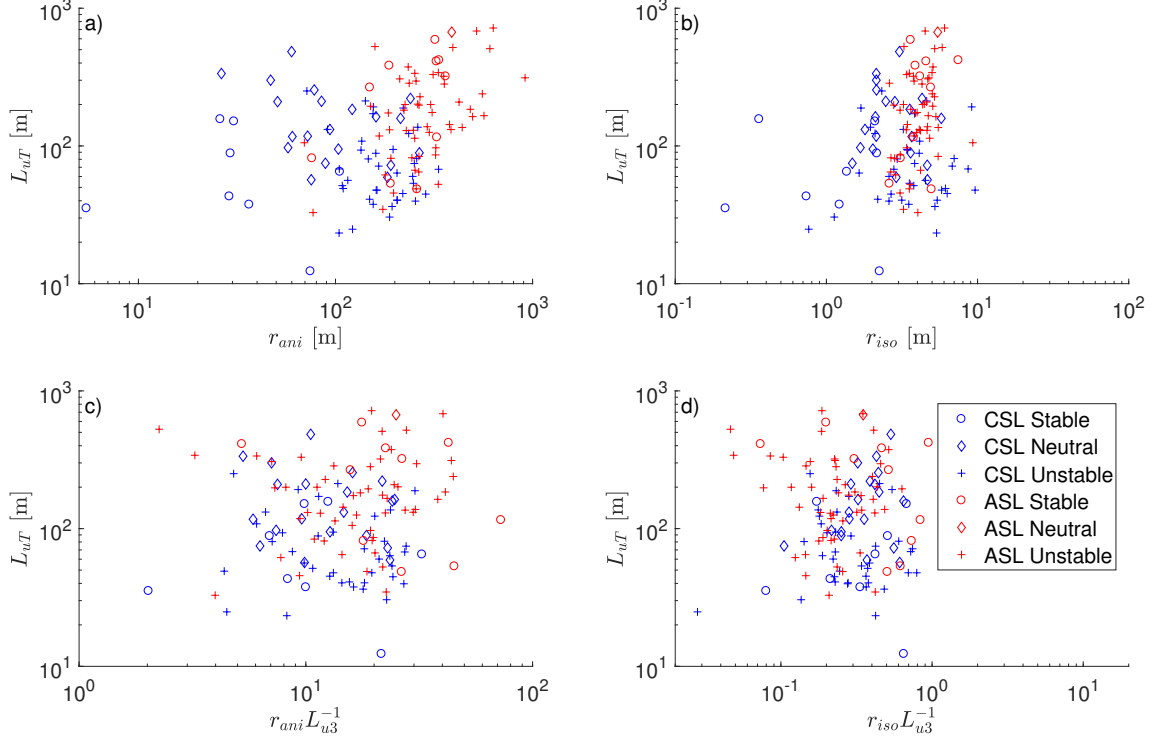


FIG. 7. The starting scales of the return-to-isotropy  $r_{ani}$  (a) and  $r_{ani} L_{u3}^{-1}$  (c) and scales  $r_{iso}$  (b) and  $r_{iso} L_{u3}^{-1}$  (d) at which isotropy is reached are plotted against the temperature length scale  $L_{uT}$ . Circles indicate stable, diamonds near neutral and crosses unstable stratification. Blue symbols show the CSL over the forest canopy and red symbols the ASL over the desert surface.

for subgrid-scale anisotropy based on explicit algebraic Reynolds stress models, which utilize the mean strain and rotation rate have been developed and successfully tested [79, 80]. Our results show that near-isotropy can be attained for fine scales ( $< 5$  m) in CSL and ASL flows, but coarser grid resolutions require anisotropic subgrid modeling. Further, the results here can be utilized to improve or formulate new wall-blocking models, for example in the description of the mean velocity profile [81], as the data set spans atmospheric flows from weak blockage (CSL) to strong blockage (ASL) and covers a wide range of velocity variances. The aforementioned examples above implicitly or explicitly assume Rotta's energy redistribution hypothesis, which is popular in higher order-closure schemes [82] used in climate and weather forecasting models (e.g. WRF). The analysis here hints to a need for exploring approaches beyond a linear Rotta scheme. Another path for improvement is to find a normalization collapsing  $r_{ani}$  between CSL and ASL, which then could be utilized in modelling an efficiency of the return-to-isotropy.

## VI. CONCLUSIONS

Scalewise invariant analysis showed that the return-to-isotropy is initiated at larger scales and covers a wider range of scales in the ASL when compared to the CSL. This statement holds when scales (or separation distances) are normalized by the integral length of the vertical velocity. The two normalized scales at which the return-to-isotropy becomes active and near-isotropy is attained are insensitive to atmospheric thermal stratification (again when the scales are normalized by the integral length scale of the vertical velocity). However, the precise trajectory in the BAM towards isotropy at finer scales is modified by thermal stratification and mean velocity gradient, and does not follow expectation from homogeneous turbulence. The analysis also reveals that larger scales appear less anisotropic in the CSL when compared to their ASL counterpart. Both CSL and ASL appear near-planar isotropic at large scales. However, the reduced overall anisotropy in the CSL mainly originates from  $\sigma_{u3}/(\sigma_{u1} + \sigma_{u2})$  being larger for CSL when compared to its ASL counterpart. Hence, CSL turbulence commences its relaxation to isotropy in BAM with reduced scales from a point closer to the 3D state and along the 2-D/3-D interface. Because of the significance

of the third invariant (in both ASL and CSL), the classical Rotta return-to-isotropy approach must be amended. The work here also shows that the return-to-isotropy depends more on surface roughness properties and less on surface heating. From a broader perspective, the work here extends prior laboratory (pipe and wind-tunnel) studies by demonstrating that rougher surfaces (i.e. a forest) tend to make turbulence more isotropic than their smooth wall or small roughness (i.e. shrubland) counterparts.

## ACKNOWLEDGMENTS

G.K. acknowledges support from the National Science Foundation (NSF-EAR-1344703, NSF-AGS-1644382,

and NSF-DGE-1068871) and from the Department of Energy (DE-SC0011461). K.K. and P.B. acknowledge support from the German Research Foundation (DFG) as part of the project “Climate feedbacks and benefits of semi-arid forests” (CliFF). M.M. and F.D.R. acknowledge support from the Helmholtz-Association through the President’s Initiative and Networking Fund as part of the Young Investigator Group “Capturing all relevant scales of biosphere-atmosphere exchange – the enigmatic energy balance closure problem”. This work was supported by a MICMoR Visiting Scientist Fellowship through KIT/IMK-IFU to G.K.

- 
- [1] A. S. Monin and A. M. F. Obukhov, “Basic laws of turbulent mixing in the surface layer of the atmosphere,” *Tr. Akad. Nauk SSSR Geophys. Inst.* **24**, 163–187 (1954), [Geophys. Inst. Acad. Sci. USSR 151.163 (1954): e187].
  - [2] A. J. Dyer, “A review of flux-profile relationships,” *Bound.-Lay. Meteorol.* **7**, 363–372 (1974).
  - [3] J. R. Garratt, “Surface influence upon vertical profiles in the atmospheric near-surface layer,” *Q. J. R. Meteorol. Soc.* **106**, 803–819 (1980).
  - [4] M. R. Raupach and A. S. Thom, “Turbulence in and above plant canopies,” *Annu. Rev. Fluid Mech.* **13**, 97–129 (1981).
  - [5] M. R. Raupach, J. J. Finnigan, and Y. Brunet, “Coherent eddies and turbulence in vegetation canopies: the mixing-layer analogy,” *Bound.-Lay. Meteorol.* **25**, 351–382 (1996).
  - [6] J. J. Finnigan, “Turbulence in plant canopies,” *Annu. Rev. Fluid Mech.* **32**, 519–571 (2000).
  - [7] T. Foken, “50 years of the Monin–Obukhov similarity theory,” *Bound.-Lay. Meteorol.* **119**, 431–447 (2006).
  - [8] I. N. Harman and J. J. Finnigan, “A simple unified theory for flow in the canopy and roughness sublayer,” *Bound.-Lay. Meteorol.* **123**, 339–363 (2007).
  - [9] G. G. Katul, A. G. Konings, and A. Porporato, “Mean velocity profile in a sheared and thermally stratified atmospheric boundary layer,” *Phys. Rev. Lett.* **107**, 268502 (2011).
  - [10] J. C. Wyngaard and O. R. Coté, “The budgets of turbulent kinetic energy and temperature variance in the atmospheric surface layer,” *J. Atmos. Sci.* **28**, 190–201 (1971).
  - [11] H. A. Panofsky and J. A. Dutton, *Atmospheric turbulence: models and methods for engineering applications*, Tech. Rep. (Wiley, 1984).
  - [12] B. A. Kader and A. M. Yaglom, “Mean fields and fluctuation moments in unstably stratified turbulent boundary layers,” *J. Fluid Mech.* **212**, 637–662 (1990).
  - [13] J. R. Garratt *et al.*, *The atmospheric boundary layer*, Cambridge atmospheric and space science series, Vol. 416 (Cambridge University Press, Cambridge).
  - [14] J. C. Kaimal and J. J. Finnigan, *Atmospheric boundary layer flows: their structure and measurement* (Oxford University Press, 1994).
  - [15] J. J. Finnigan, R. H. Shaw, and E. G. Patton, “Turbulence structure above a vegetation canopy,” *J. Fluid Mech.* **637**, 387–424 (2009).
  - [16] T. Banerjee and G. G. Katul, “Logarithmic scaling in the longitudinal velocity variance explained by a spectral budget,” *Phys. Fluids* **25**, 125106 (2013).
  - [17] T. Banerjee, G. G. Katul, S. T. Salesky, and M. Chamecki, “Revisiting the formulations for the longitudinal velocity variance in the unstable atmospheric surface layer,” *Q. J. R. Meteorol. Soc.* **141**, 1699–1711 (2015).
  - [18] T. Banerjee, D. Li, J.-Y. Juang, and G. G. Katul, “A spectral budget model for the longitudinal turbulent velocity in the stable atmospheric surface layer,” *J. Atmos. Sci.* **73**, 145–166 (2016).
  - [19] E. G. Patton, P. P. Sullivan, R. H. Shaw, J. J. Finnigan, and J. C. Weil, “Atmospheric stability influences on coupled boundary layer and canopy turbulence,” *J. Atmos. Sci.* **73**, 1621–1647 (2016).
  - [20] R. A. Antonia, J. Kim, and L. W. B. Browne, “Some characteristics of small-scale turbulence in a turbulent duct flow,” *J. Fluid Mech.* **233**, 369–388 (1991).
  - [21] H. S. Shafi and R. A. Antonia, “Anisotropy of the Reynolds stresses in a turbulent boundary layer on a rough wall,” *Exp. Fluids* **18**, 213–215 (1995).
  - [22] K. S. Choi and J. L. Lumley, “The return to isotropy of homogeneous turbulence,” *J. Fluid Mech.* **436**, 59–84 (2000).
  - [23] P.-Å. Krogstad and L. E. Torbergsen, “Invariant analysis of turbulent pipe flow,” *Flow, Turbul. Combust.* **64**, 161–181 (2000).
  - [24] R. A. Antonia and P.-Å. Krogstad, “Turbulence structure in boundary layers over different types of surface roughness,” *Fluid Dynamics Research* **28**, 139–157 (2001).
  - [25] R. Smalley, S. Leonardi, R. Antonia, L. Djenidi, and P. Orlandi, “Reynolds stress anisotropy of turbulent rough wall layers,” *Exp. Fluids* **33**, 31–37 (2002).
  - [26] H. Liu, R. Yuan, J. Mei, J. Sun, Q. Liu, and Y. Wang, “Scale properties of anisotropic and isotropic turbulence in the urban surface layer,” *Bound.-Lay. Meteorol.* **165**, 277–294 (2017).

- [27] S. Sarkar and C. G. Speziale, "A simple nonlinear model for the return to isotropy in turbulence," *Phys. Fluids A* (1989-1993) **2**, 84–93 (1990).
- [28] P. K. Yeung and James G. Brasseur, "The response of isotropic turbulence to isotropic and anisotropic forcing at the large scales," *Phys. Fluids A* **3**, 884–897 (1991).
- [29] T. Jongen and T. B. Gatski, "General explicit algebraic stress relations and best approximation for three-dimensional flows," *Int. J. Eng. Sci. (Oxford, U. K.)* **36**, 739–763 (1998).
- [30] F. G. Schmitt, "Direct test of a nonlinear constitutive equation for simple turbulent shear flows using DNS data," *Communications in Nonlinear Science and Numerical Simulation* **12**, 1251–1264 (2007).
- [31] J. P. Panda, H. V. Warrior, S. Maity, A. Mitra, and K. Sasmal, "An improved model including length scale anisotropy for the pressure strain correlation of turbulence," *J. Fluids Eng.* **139**, 044503 (2017).
- [32] S. Banerjee, R. Krahl, F. Durst, and C. Zenger, "Presentation of anisotropy properties of turbulence, invariants versus eigenvalue approaches," *Journal of Turbulence*, N32 (2007).
- [33] J. L. Lumley and G. R. Newman, "The return to isotropy of homogeneous turbulence," *J. Fluid Mech.* **82**, 161–178 (1977).
- [34] J. L. Lumley, "Computational modeling of turbulent flows," *Adv. Appl. Mech.* **18**, 213 (1978).
- [35] T.-H. Shih, J. Zhu, and J. L. Lumley, "A new Reynolds stress algebraic equation model," *Computer Methods in Applied Mechanics and Engineering* **125**, 287–302 (1995).
- [36] D. B. Taulbee, "An improved algebraic Reynolds stress model and corresponding nonlinear stress model," *Phys. Fluids A* (1989-1993) **4**, 2555–2561 (1992).
- [37] T. Rung, F. Thiele, and S. Fu, "On the realizability of nonlinear stress-strain relationships for Reynolds stress closures," *Flow, Turbul. Combust.* **60**, 333–359 (1998).
- [38] U. Schumann, "Realizability of Reynolds-stress turbulence models," *Phys. Fluids* (1958-1988) **20**, 721–725 (1977).
- [39] D. Poggi, A. Porporato, L. Ridolfi, J. D. Albertson, and G. G. Katul, "The effect of vegetation density on canopy sub-layer turbulence," *Bound.-Lay. Meteorol.* **111**, 565–587 (2004).
- [40] J. M. Chacin and B. J. Cantwell, "Dynamics of a low Reynolds number turbulent boundary layer," *J. Fluid Mech.* **404**, 87–115 (2000).
- [41] S. B. Pope, "A more general effective-viscosity hypothesis," *J. Fluid Mech.* **72**, 331–340 (1975).
- [42] G. I. Taylor, "The spectrum of turbulence," in *Proceedings of the Royal Society of London A: Mathematical, Physical and Engineering Sciences*, Vol. 164 (The Royal Society, 1938) pp. 476–490.
- [43] C.-I. Hsieh and G. G. Katul, "Dissipation methods, Taylor's hypothesis, and stability correction functions in the atmospheric surface layer," *J. Geophys. Res.: Atmos.* **102**, 16391–16405 (1997).
- [44] E. Rotenberg and D. Yakir, "Distinct patterns of changes in surface energy budget associated with forestation in the semiarid region," *Glob. Change Biol.* **17**, 1536–1548 (2011).
- [45] F. Eder, F. De Roo, E. Rotenberg, D. Yakir, H. P. Schmid, and M. Mauder, "Secondary circulations at a solitary forest surrounded by semi-arid shrubland and their impact on eddy-covariance measurements," *Agric. For. Meteorol.* **211**, 115–127 (2015).
- [46] A. M. Obukhov, "The local structure of atmospheric turbulence," *Dokl. Akad. Nauk. SSSR* **67**, 643–646 (1949).
- [47] U. Höglström and A.-S. Smedman, "Accuracy of sonic anemometers: laminar wind-tunnel calibrations compared to atmospheric in situ calibrations against a reference instrument," *Bound.-Lay. Meteorol.* **111**, 33–54 (2004).
- [48] R. G. Barry and R. J. Chorley, *Atmosphere, weather and climate*, 8th ed. (Routledge, 29 West 35th Street, New York, NY 10001, 2003) 421 pp.
- [49] U. Dayan and J. Rodnizki, "The temporal behavior of the atmospheric boundary layer in Israel," *J. Appl. Meteorol.* **38**, 830–836 (1999).
- [50] T. Foken and B. Wichura, "Tools for quality assessment of surface-based flux measurements," *Agric. For. Meteorol.* **78**, 83–105 (1996).
- [51] M. Mauder, M. Cuntz, C. Drüe, A. Graf, C. Rebmann, H. P. Schmid, M. Schmidt, and R. Steinbrecher, "A strategy for quality and uncertainty assessment of long-term eddy-covariance measurements," *Agric. For. Meteorol.* **169**, 122–135 (2013).
- [52] J. C. Isaza and L. R. Collins, "On the asymptotic behaviour of large-scale turbulence in homogeneous shear flow," *J. Fluid Mech.* **637**, 213–239 (2009).
- [53] I. Marusic, J. P. Monty, M. Hultmark, and A. J. Smits, "On the logarithmic region in wall turbulence," *J. Fluid Mech.* **716**, R3 (2013).
- [54] C. Meneveau and I. Marusic, "Generalized logarithmic law for high-order moments in turbulent boundary layers," *J. Fluid Mech.* **719** (2013).
- [55] R. J. A. M. Stevens, M. Wilczek, and C. Meneveau, "Large-eddy simulation study of the logarithmic law for second-and higher-order moments in turbulent wall-bounded flow," *J. Fluid Mech.* **757**, 888–907 (2014).
- [56] T. Banerjee, P. Brugger, F. De Roo, K. Kröniger, D. Yakir, E. Rotenberg, and M. Mauder, "Turbulent transport of energy across a forest and a semi-arid shrubland," *Atmospheric Chemistry and Physics Discussion* **2017**, 1–21 (2017).
- [57] G. G. Katul and W.-H. Chang, "Principal length scales in second-order closure models for canopy turbulence," *J. Appl. Meteorol.* **38**, 1631–1643 (1999).
- [58] B. A. Kader, A. M. Yaglom, and S. L. Zubkovskii, "Spatial correlation functions of surface-layer atmospheric turbulence in neutral stratification," *Bound.-Lay. Meteorol.* **47**, 233–249 (1989).
- [59] Y. Pan and M. Chamecki, "A scaling law for the shear-production range of second-order structure functions," *J. Fluid Mech.* **801**, 459–474 (2016).
- [60] P. Drobinski, P. Carlotti, R. K. Newsom, R. M. Banta, R. C. Foster, and J.-L. Redelsperger, "The structure of the near-neutral atmospheric surface layer," *J. Atmos. Sci.* **61**, 699–714 (2004).
- [61] P. A. Davidson, T. B. Nickels, and P.-Å Krogstad, "The logarithmic structure function law in wall-layer turbulence," *J. Fluid Mech.* **550**, 51–60 (2006).
- [62] P. A. Davidson and P.-Å Krogstad, "A simple model for the streamwise fluctuations in the log-law region of a boundary layer," *Phys. Fluids* **21**, 055105 (2009).
- [63] G. G. Katul, A. Porporato, and V. Nikora, "Existence of  $k^{-1}$  power-law scaling in the equilibrium regions of wall-bounded turbulence explained by heisenberg's eddy



- viscosity,” *Phys. Rev. E* **86**, 066311 (2012).
- [64] G. G. Katul, T. Banerjee, D. Cava, M. Germano, and A. Porporato, “Generalized logarithmic scaling for high-order moments of the longitudinal velocity component explained by the random sweeping decorrelation hypothesis,” *Phys. Fluids* **28**, 095104 (2016).
- [65] P. A. Davidson and P.-Å. Krogstad, “A universal scaling for low-order structure functions in the log-law region of smooth-and rough-wall boundary layers,” *J. Fluid Mech.* **752**, 140–156 (2014).
- [66] C. M. de Silva, I. Marusic, J. D. Woodcock, and C. Meneveau, “Scaling of second-and higher-order structure functions in turbulent boundary layers,” *J. Fluid Mech.* **769**, 654–686 (2015).
- [67] R. A. Antonia and M.R. Raupach, “Spectral scaling in a high Reynolds number laboratory boundary layer,” *Bound.-Lay. Meteorol.* **65**, 289–306 (1993).
- [68] Marcelo Chamecki, Nelson L. Dias, Scott T. Salesky, and Ying Pan, “Scaling laws for the longitudinal structure function in the atmospheric surface layer,” *J. Atmos. Sci.* **74**, 1127–1147 (2017).
- [69] J. C. Kaimal, J. C. Wyngaard, Y. Izumi, and O. R. Cot, “Spectral characteristics of surface-layer turbulence,” *Q. J. R. Meteorol. Soc.* **98**, 563–589 (1972).
- [70] G. G. Katul, C.-I. Hsieh, and J. Sigmon, “Energy-inertial scale interactions for velocity and temperature in the unstable atmospheric surface layer,” *Bound.-Lay. Meteorol.* **82**, 49–80 (1997).
- [71] J. C. Wyngaard and S. F. Clifford, “Taylor’s hypothesis and high-frequency turbulence spectra,” *J. Atmos. Sci.* **34**, 922–929 (1977).
- [72] F. Toschi, E. Leveque, and G. Ruiz-Chavarria, “Shear effects in nonhomogeneous turbulence,” *Phys. Rev. Lett.* **85**, 1436 (2000).
- [73] D. Poggi, A. Porporato, and L. Ridolfi, “Analysis of the small-scale structure of turbulence on smooth and rough walls,” *Phys. Fluids* **15**, 35–46 (2003).
- [74] G. G. Katul, A. Porporato, C. Manes, and C. Meneveau, “Co-spectrum and mean velocity in turbulent boundary layers,” *Phys. Fluids* **25**, 091702 (2013).
- [75] T. Ishihara, K. Yoshida, and Y. Kaneda, “Anisotropic velocity correlation spectrum at small scales in a homogeneous turbulent shear flow,” *Phys. Rev. Lett.* **88**, 154501 (2002).
- [76] J. W. Deardorff, “Stratocumulus-capped mixed layers derived from a three-dimensional model,” *Bound.-Lay. Meteorol.* **18**, 495–527 (1980).
- [77] C.-H. Moeng and J. C. Wyngaard, “Spectral analysis of large-eddy simulations of the convective boundary layer,” *J. Atmos. Sci.* **45**, 3573–3587 (1988).
- [78] B. Maronga, M. Gryschka, R. Heinze, F. Hoffmann, F. Kanani-Sühring, M. Keck, K. Ketelsen, M. O. Letzel, M. Sühring, and S. Raasch, “The parallelized large-eddy simulation model (palm) version 4.0 for atmospheric and oceanic flows: model formulation, recent developments, and future perspectives,” *Geoscientific Model Development* **8**, 2515 (2015).
- [79] T. B. Gatski and C. G. Speziale, “On explicit algebraic stress models for complex turbulent flows,” *J. Fluid Mech.* **254**, 59–78 (1993).
- [80] L. Marstorp, G. Brethouwer, O. Grundestam, and A. V. Johansson, “Explicit algebraic subgrid stress models with application to rotating channel flow,” *J. Fluid Mech.* **639**, 403–432 (2009).
- [81] K. A. McColl, G. G. Katul, P. Gentile, and D. Entekhabi, “Mean-velocity profile of smooth channel flow explained by a cospectral budget model with wall-blockage,” *Physics of Fluids* **28**, 035107 (2016).
- [82] G. L. Mellor and T. Yamada, “Development of a turbulence closure model for geophysical fluid problems,” *Reviews of Geophysics* **20**, 851–875 (1982).